脳梁軸索投射ニューロンは特異的な資格応答と局所結合様式を示す

萩原, 賢太

Title: Long-range interhemispheric projection neurons show biased response properties and fine-scale local subnetworks in mouse visual cortex

Running title: Response and connectivity profiles of visual callosal neurons

Authors: Kenta M. Hagihara[1, 10*#], Ayako Wendy Ishikawa[2, 3, 11*], Yumiko Yoshimura[2, 3], Yoshiaki Tagawa[4, 5, 6], and Kenichi Ohki[1, 6, 7, 8, 9]

Author Affiliation:

[1] Department of Molecular Physiology, Kyushu University Graduate School of Medical Sciences, 3-1-1, Maidashi, Higashi-Ku, Fukuoka 812-8582, Japan

[2] Division of Visual Information Processing, National Institute for Physiological Sciences, National Institutes of Natural Sciences, Okazaki 444-8585, Japan.

[3] Department of Physiological Sciences, The Graduate University for Advanced Studies, Okazaki 444-8585, Japan.

[4] Department of Biophysics, Kyoto University Graduate School of Science, Kitashirakawa-Oiwake-cho, Sakyo-ku, Kyoto 606-8502, Japan

[5] Department of Physiology, Graduate School of Medical and Dental Sciences, Kagoshima University, 8-35-1, Sakuragaoka, Kagoshima 890-8544, Japan

[6] CREST, Japan Science and Technology Agency, Kawaguchi, Saitama 332-0012, Japan

[7] Department of Physiology, [8] International Research Center for Neurointelligence (IRCN), [9] Beyond AI Institute, The University of Tokyo School of Medicine, 7-3-1 Hongo, Bunkyo-ku, Tokyo 113-0033, Japan

[10] Present address: Friedrich Miescher Institute for Biomedical Research, Basel, 4058, Switzerland

[11] Present address: Keio University School of Medicine, Shinanomachi, Shinjuku-ku, 160-8582, Japan

*: These authors contributed equally to this work

#: Correspondence to: Kenta M. Hagihara (hagi_k@med.kyushu-u.ac.jp; kenta-hagihara@umin.ac.jp)

Number of pages: 30; Number of figures: 3; Number of supplementary figures: 5;

Conflict of Interest: The authors declare no competing financial interests.

Abstract

Integration of information processed separately in distributed brain regions is essential for brain functions. This integration is enabled by long-range projection neurons, and further, concerted interactions between long-range projections and local microcircuits are crucial. It is not well known, however, how this interaction is implemented in cortical circuits. Here, to decipher this logic, using callosal projection neurons (CPNs) in layer 2/3 of the mouse visual cortex as a model of long-range projections, we found that CPNs exhibited distinct response properties and fine-scale local connectivity patterns. *In vivo* 2-photon calcium imaging revealed that CPNs showed a higher ipsilateral (to their somata) eye preference, and that CPN pairs showed stronger signal/noise correlation than random pairs. Slice recordings showed CPNs were preferentially connected to CPNs, demonstrating the existence of projection target-dependent fine-scale subnetworks. Collectively, our results suggest that long-range projection target predicts response properties and local connectivity of cortical projection neurons.

Keywords: Callosal projection neuron; visual cortex; ocular dominance; 2-photon imaging; slice physiology

Introduction

The cerebral cortex processes information arriving from the external world in a distributed

manner. To achieve this, there must be biophysical substrates enabling proper routing, local computation, and integration of information. Integration of distributed information is mediated by cortical projection neurons; thus, the functional organization of these neurons have been extensively studied (Glickfeld et al., 2013; Kim et al., 2015; Lur et al., 2016; Movshon and Newsome, 1996; Sato and Svoboda, 2010; Yamashita et al., 2013). Such studies have revealed that as a general principle, neurons projecting to different areas encode different features of the sensory input. In addition, fine-scale local network motifs (Brown and Hestrin, 2009; Kampa et al., 2006; Otsuka and Kawaguchi, 2011; Yoshimura et al., 2005) implicated in selective local computation have been identified. Recent work has found that cortical neurons that do not share their projection targets are rarely connected to each other, suggesting the existence of strongly segregated local network motifs suited for highly selective information transmission (Kim et al., 2018). However, the organizational principles linking projection targets to functional properties and fine-scale local networks have not been fully addressed. More specifically, whether the strongly segregated local network is the general motif for all the long-range projection populations is an open question to be addressed.

Callosal projection neurons (CPNs) are essential for integrating information processed in separate hemispheres (Hubel and Wiesel, 1967; Van Essen et al., 1982), and thus serve as an ideal model to study the functional organization of long-range projection neurons. Although many lesion and inactivation studies have been performed, to what extent callosal inputs influence the visual response properties of primary visual cortex (V1) neurons is still controversial (Berlucchi and Rizzolatti, 1968; Cerri et al., 2010; Dehmel and Lowel, 2014; Minciacchi and Antonini, 1984; Payne et al., 1980; Ramachandra et al., 2020;

Restani et al., 2009; Schmidt et al., 2010; Wunderle et al., 2013; Zhao et al., 2013). Due to the lack of a method enabling selective *in vivo* recordings from CPNs and non-CPNs, the specific visual information encoded and transmitted by individual CPNs remains largely unknown. Considering the versatility of CPNs as experimental models such as for cortical area identification (Wang and Burkhalter, 2007), for optogenetic circuit mapping *in vitro* (Petreanu et al., 2007), for antidromic optogenetic stimulation *in vivo* (Sato et al., 2014), for studying bilaterally concerted behavior such as eye-movement (Itokazu et al., 2018; Sato et al., 2019), and for developmental circuit formation (Mizuno et al., 2007), functional characterization of CPNs itself is also of high interest.

In higher mammals such as cats and monkeys, the inputs from each eye are spatially segregated in V1 as ocular dominance columns (Van Essen et al., 1992; Wiesel and Hubel, 1965). On the other hand, rodents, especially mice have no ocular dominance columns ((Antonini et al., 1999; Drager, 1974; Gordon and Stryker, 1996; Mrsic-Flogel et al., 2007; Scholl et al., 2015) but see (Laing et al., 2015) for results in the Long Evans rat) rather, functionally distinct neuronal populations are spatially organized in a "salt and pepper" manner (Ohki and Reid, 2007). Thus, to assess the relationships between CPN response properties and local connection patterns, it is crucial to assess neuronal responses and local connectivity at single-cell resolution and to directly compare the functional organization of CPNs to surrounding non-CPNs. Here, we achieve this by combining retrograde-labeling of CPNs with *in vivo* two-photon calcium imaging and *ex vivo* slice recordings in layer 2/3 (L2/3) of the mouse visual cortex.

Materials and Methods

LEAD CONTACT AND MATERIALS AVAILABILITY

Further information and requests for resources and reagents should be directed to and will be fulfilled by the Lead Contact, Kenta M. Hagihara (hagi_k@med.kyushu-u.ac.jp; kenta-hagihara@umin.ac.jp).

EXPERIMENTAL MODEL AND SUBJECT DETAILS

All of the experiments were performed in accordance with the institutional animal welfare guidelines of the Animal Care and Use Committee of Kyushu University, Kyoto University and National Institute for Physiological Sciences, and they were approved by the Ethical Committee of Kyushu University, the local committee for handling experimental animals in the Graduate School of Science, Kyoto University, and National Institute for Physiological Sciences.

METHOD DETAILS

Stereotactic retrograde tracer injection for imaging experiments and histology

Mice (C57BL/6, both males and females, aged at postnatal day 60-90) were housed in the temperature-controlled animal room with 12h/12h light/dark cycle. Cholera Toxin Subunit B Alexa Fluor 555 or 488 Conjugate (CTB555 or CTB488, 1.0%, weight/volume, Invitrogen) and Green Retrobeads™ IX (Green Beads, Lumafluor Inc.) were used as retrograde tracers (Conte et al., 2009; Li et al., 2015). The mice were subjected to stereotactic tracer injections using pulled glass micropipettes. The mice were anesthetized with 440 mg/kg chloral hydrate (Tokyo Chemical Industry) by intraperitoneal injection. The mice were then fixed to a small-animal stereotactic device (Narishige). The head skin was cut at the midline, and the periosteum was removed using a surgical knife. The skull was thinned with a drill, and a small craniotomy was made using a 30- gauge needle. The tracer was injected through a pulled glass micropipette connected to a Hamilton syringe (Hamilton Company), which was pumped using a syringe pump device (World Precision Instruments). The stereotactic

injections were administered at BZ. The stereotaxic coordinates for BZ injection were 3.5 mm lateral of the midline and 2.0 mm in front of the anterior margin of the transverse sinus. The tracer solution was injected at a rate of 0.05–0.1 µl/min at a volume of 2.0 µl to cover most of BZ (**Figure S1A**), and after the injection, the pipette was held in place for an additional 10 min before removal. After the removal of the micropipette, the skin incision was sutured. The post-injection animals were housed normally for 5–14 days before imaging or histology experiments. Fluorescent histological images were acquired using a confocal laser-scanning microscope (LSM700, Zeiss).

In the experiment described in **Figure S2**, a cocktail of Green Beads and CTB555 (1.0%) was used. Given the efficiency (0-1) of Green Beads and of CTB555 as *a* and *b*, respectively, and the fraction of CPNs as *n*, the fraction of CPNs labeled with both Green Beads and CTB555 would be *n*a*b*. Considering that neurons labeled with Green Beads were also mostly labeled with CTB555, here n**a*b* can be regarded as near *n*a* and thus *b* can be regarded as 1. Thus, in this system, the efficiency of CTB555 can be regarded as almost 100% and neurons not labeled with CTB555 can be regarded as non-CPNs.

Stereotactic retrograde tracer injection for slice experiments

For retrograde labeling of CPNs, 28–32-day old C57BL/6 mice of either sex were anesthetized with propofol (0.2%, 100 ml/kg ip, Maruishi) and then fixed to a small-animal stereotactic device. CTB488 or CTB555 (300–500 nl) was pressure-injected (Toohey Spritzer microinjector, Toohey Company) into the visual cortex contralateral to the eventual recording site (3.5 mm lateral to the midline, 1.5 mm rostral to the anterior margin of the transverse sinus, 300–600 µm in depth) with pulled glass pipettes (tip diameter 10–20 µm,

170 Narishige) to cover most of BZ. The pipette was held in place for 10 min before and after
171 injection. After removal of the pipette, the skin incision was sutured and mice were allowed
172 to recover for 4–8 days before recording.
173
174 *Animal preparation and surgery for in vivo calcium imaging*
175 5-14 days after CTB555 injection, the animals were prepared for *in vivo* calcium imaging as
176 previously described (Hagihara et al., 2015; Ohki and Reid, 2014). In brief, mice were
177 anesthetized with isoflurane, then a custom-made metal plate was mounted on the skull,
178 and a craniotomy was carefully performed on the other hemisphere above the area where
179 fluorescence from CTB555 was clearly observed through the skull. We dissolved 0.8 mM
180 Oregon Green 488 BAPTA-1 AM (OGB1) in DMSO with 20% pluronic acid and mixed it with
181 ACSF containing 0.05 mM Alexa594 (all obtained from Invitrogen). A glass pipette (3–5 μm
182 tip diameter) was filled with this solution and inserted into the cortex, and OGB1 and Alexa
183 were pressure-ejected from the pipette (–2 psi for 300–500 ms, 10–20 times). After
184 confirming loading, the craniotomy was sealed with a cover glass. 281.6 μm×281.6 μm area
185 was imaged using a two-photon microscope (Nikon A1MP, Nikon), which was equipped
186 with a mode-locked Ti:sapphire laser (MaiTai Deep See, Spectra Physics) at 2 Hz with
187 512×512 pixels (0.55 μm/pixel). The excitation light was focused with a 25× Nikon (NA: 1.10)
188 PlanApo objective. The average power delivered to the brain was < 20 mW, depending on
189 the depth of focus. OGB1 and CTB555 were excited at 1000 nm except for the experiment
190 using 920 nm described in **Figure S1B**. The emission filters were 517–567 nm for OGB-1 and
191 600–650 nm for CTB555.

192

193 *Visual stimulation and image data acquisition*

194 The visual stimulation for studying the binocular response property was performed using
195 two LEDs controlled by Arduino (Smart Projects). To avoid contamination to the other eye,
196 LEDs were directly attached to the eyes with black silicon. Intensity was set as 40 cd/m^2. Each
197 stimulus started with a blank period (4s), which was followed by visual stimulation (4s). Each
198 stimulus was consisted of 4 rounds of alternative 0.5 seconds of ON and OFF periods. We
199 used 410 nm LED stimuli, based on the report that all mouse photoreceptors display similar
200 sensitivity to spectrum around 400 nm (Govardovskii et al., 2000). Our measures of
201 sensitivity are thus not biased towards responses originating from any specific
202 photoreceptor. In particular, the dorsal-ventral gradient in cone-opsin expression in the
203 mouse retina (Applebury et al., 2000; Sterratt et al., 2013) is not likely to have influence with
204 our measures of relative sensitivity. To study orientation and direction selectivity, drifting
205 square-wave gratings (100% contrast, 2 Hz temporal frequency) were presented in 12
206 directions of motion with 30 degree steps on a 27-inch LCD monitor (Samsung, Hwaseong,
207 South Korea) placed in 20 cm distance from eyes. We positioned the center of the monitor
208 to cover the vertical meridian. The drifting gratings visual stimulus sets were generated
209 using custom-made software written in PsychoPy (Peirce, 2007). The spatial frequency was
210 set at 0.03 cycles per degree. Each stimulus started with a blank period of uniform gray with
211 the same mean luminance of gratings (4s), which was followed by visual stimulation (4s).
212 For mapping of spatial frequency (SPF) and temporal frequency (TF) tunings, drifting sine-
213 wave gratings (100% contrast) were used. For SPF mapping experiments, sine-wave
214 gratings with six SPFs between 0.01 cycle per degree (cpd) and 0.32 cpd in octave steps,

drifting at 2 Hz were used. For TF mapping experiments, sine-wave gratings having 0.04 cpd and drifting at 5 different TFs between 0.5 and 8 Hz in octave steps were used. Each stimulus started with a blank period of uniform gray (4 s) followed by the same period of visual stimulation during vertical and horizontal gratings were presented for 1 s for each of four directions (0°, 180°, 90°, and 270° in that order). These 3 drifting grating stimulus sets were repeated 10 times.

Slice experiments

Coronal slices (300 μm thick) containing visual cortex were prepared from mice at postnatal day 32–36 following deep anesthesia with isoflurane. At this age, binocular matching of orientation preference in V1 neurons reaches the adult level, suggesting that binocular visual functions in V1 are mature (Wang et al., 2010). Prior to recording, slices were incubated for 1 h in oxygenated (95% O_2 and 5% CO_2) normal artificial cerebrospinal fluid (ACSF) containing (in mM) 126 NaCl, 3 KCl, 1.3 $MgSO_4$, 2.4 $CaCl_2$, 1.2 NaH_2PO_4, 26 $NaHCO_3$, and 10 glucose at 33ºC as described previously (Ishikawa et al., 2014). Neurons with pyramidal shaped somata in L2/3 were targeted by patch pipettes under fluorescent and infrared differential interference contrast (DIC) optics with a 60X water immersion objective (BX51, Olympus, Tokyo, Japan, **Figure 3A**). Pyramidal neurons retrogradely labeled with CTB488 or CTB555 were identified by epifluorescence with appropriate filter sets (U-MWIB3: excitation 479–495 nm and emission 510IF nm for CTB488; U-MWIG3: excitation 530–550 nm and emission 575IF nm for CTB555). We performed whole-cell recordings from pairs of L2/3 pyramidal neurons at room temperature. In all three groups (CPN-CPN pairs, CPN-non CPN pairs, and non-CPN pairs), we recorded from pairs of neurons with somata separated within approximately 70 μm. We analyzed only neurons showing regular spiking firing

patterns with a transient high-frequency firing at an initial phase followed by a low-frequency firing for the rest of the response (**Figure S5A)**. Cell bodies of the recorded neurons were located >50 μm below the cut surface of the slice. The patch pipettes (4–6 MΩ) were filled with an internal solution containing (in mM) 130 K-gluconate, 8 KCl, 1 $MgCl_2$, 0.6 EGTA, 10 HEPES, 3 MgATP, 0.5 Na_2GTP and 10 Na-phosphocreatine (pH 7.3, adjusted using KOH). The presence of synaptic connections between recorded neuron pairs was tested by applying brief depolarizing voltage pulses (duration, 1–2 ms) to evoke an action potential in one cell (≥ 50 trials) and recording excitatory postsynaptic currents (EPSCs) from the other cell (Ishikawa et al., 2014). Connection probabilities were calculated as the number of unidirectionally or reciprocally connected neuron pairs over the number of recorded neuron pairs. In the voltage-clamp mode, a brief, large depolarization pulse applied to the soma initiates an action potential at the axon because of the imperfect space clamp. The membrane potential of recorded cells was held at the reversal potential of IPSCs (–70 mV) after correction of liquid junction potential. Recordings were made using a Multiclamp 700B amplifier, Digidata 1440A converter, and pCamp10 software (all from Molecular Devices).

Data were digitized at 10 kHz, filtered at 1 kHz, and analyzed using custom-made programs written in MATLAB. To obtain the amplitude of EPSCs, we averaged the peak values of individual EPSCs after excluding failures. The baseline current was defined as the averaged current in a 5-ms window before application of depolarizing voltage pulses to the presynaptic cell. The peak EPSC was defined as the peak current minus the baseline. We selected cells with seal resistance >1 GΩ and series resistance <35 MΩ for analysis. For measuring intrinsic membrane properties of neurons, 1-s step currents from –100 pA to 500 pA in 25 pA increments were injected in current clamp mode. The current injection

experiments were conducted within 5 min after establishing the whole-cell patch-clamp configuration.

QUANTIFICATION AND STATISTICAL ANALYSIS

Data analysis of visual response

The images were analyzed by using our custom-written in-house software running on MATLAB (Mathworks) as previously described (Hagihara et al., 2015; Ohki et al., 2005). In brief, the cell outlines were automatically identified using template matching. The identified cell outlines were visually inspected, and the rare but clear errors were manually corrected. The time courses of individual cells were extracted by summing the pixel values within the cell outlines. Slow drift of the time courses over minutes, potentially caused by gradual z-movement, bleaching, and/or diffusion of OGB1, was removed by applying a low-cut filter (cut-off, 2–4 min). The baseline (F) for each trial with each cell was calculated by averaging the values of the last 0.5 s of the blank periods for all stimuli. Neuropil contamination was removed as previously described (Hagihara et al., 2015; Kerlin et al., 2010). Visually responsive cells were defined by ANOVA ($P < 0.01$) across blank and 2 eyes (for ocular dominance stimuli), across blank and 12 direction periods (for orientation/direction stimuli), across blank and 6 SPF/TF periods (for SPF/TF stimuli), where $\Delta F/F>2\%$. Instead of $P < 0.05$, $P < 0.01$ was used here, to reduce false positives due to large sample size of neurons.

For responsive cells with ocular dominance stimuli, ODscore (Mrsic-Flogel et al., 2007) was defined as follows: (response to ipsilateral-eye)/(response to ipsilateral-eye) +

(response to contralateral-eye). For responsive cells with drifting grating stimuli, as an index for orientation selectivity tuning, gOSI was calculated. This value is equivalent to :((Sigma $R(\theta_i)\sin(2\theta i))^2$ + (Sigma $R(\theta i)\cos(2\theta i))^2)^{(1/2)}$/Sigma $R(\theta i)$, where θi is the orientation of each stimulus and $R(\theta_i)$ is the response to that stimulus. For direction selectivity, DI was calculated as :1 – (response to null direction)/(response to preferred direction). The preferred orientation and direction were defined by vector averaging of responses (ΔF/F) to all orientations and directions, respectively. For correlation analysis, Pearson's correlation coefficient was calculated to obtain pair-wises response correlation. Signal correlation was calculated as the correlation coefficient between the trial-averaged traces in responses to the ocular dominance stimulus. Noise correlation was obtained by subtracting the trial-averaged traces from the traces to each trial, and then calculating the correlation coefficient between those mean-subtracted traces. Note that the same analysis based on responses to drifting gratings data gave consistent results (**Figure S4C, D**).

Statistical analyses

All data are expressed as the mean ± standard error of the mean (SEM), unless stated otherwise. The two-sided Wilcoxon signed-rank test was used to compare two paired groups. Friedman test was performed when more than two groups were compared. When significant, it was followed by Tukey-Kramer method. For distribution of preferred orientation and direction, Kolmogorov-Smirnov test was used. For data from slice whole-cell patch clamp recordings, Wilcoxon rank-sum test was used to compare two groups. Fisher's exact test was used to compare the proportions of connected cell pairs. Kruskal-Wallis test was used when more than two groups were compared. The variances between

groups were assumed to be similar. Throughout the study, $P < 0.05$ was considered statistically significant, other than the definitions of visually responsive and selective cells (see Data analysis of visual response). No statistical methods were used to pre-determine sample sizes, but our sample sizes are similar to those generally employed in the field.

DATA AND SOFTWARE AVAILABILITY

All data and analysis code are available upon reasonable request to the Lead Contact, Kenta M. Hagihara (hagi_k@med.kyushu-u.ac.jp; kenta-hagihara@umin.ac.jp).

Results

To compare the visual response properties of CPNs and non-CPNs in L2/3 of mouse visual cortex, we performed *in vivo* two-photon calcium imaging (Ohki et al., 2005). Using visual stimulation to each eye, we first assessed the ocular dominance response properties of CPNs and non-CPNs. The fluorescent retrograde tracer cholera toxin B subunit conjugated to the fluorophore Alexa 555 (CTB555) was used to label CPNs (**Figure 1A, B, Methods)**. As Oregon Green BAPTA-1 (OGB1) injection was also performed to largely cover the CTB555-positive region along the medial–lateral axis, our recordings equally contained binocular regions of V1 and lateral secondary visual cortex (more specifically LM (Wang and Burkhalter, 2007)). We imaged 1,866 CPNs and 11,399 non-CPNs from 7 mice. There was no difference in the fraction of visually responsive CPNs and non-CPNs (31.3% ± 1.8% vs. 28.9% ± 2.2%, $P = 0.30$, Wilcoxon signed-rank test, $n = 7$ mice). Note lower responsiveness than previous reports using drifting gratings (also see **Figure 1F**). Based on fluorescence signal changes in response to unilateral visual inputs, we calculated the ocular dominance (OD) score (see **Methods** and (Mrsic-Flogel et al., 2007)) for all visually responsive neurons. Surprisingly, some CPNs showed exclusive ipsilateral eye preference (**Figure 1C**). While OD scores varied extensively for both CPNs and non-CPNs, the proportion of neurons exhibiting a high OD score (with ipsilateral eye preference) was larger in CPNs than non-CPNs (**Figure 1D**). Indeed,

a significantly larger fraction of CPNs had OD scores >0.8 compared to non-CPNs (**Figure 1E,** P = 0.016, Wilcoxon signed-rank test, n = 7 mice), while there was no significant difference in the fraction of OD scores <0.2 (P = 0.47). As previously reported in mice (Antonini et al., 1999; Drager, 1974; Gordon and Stryker, 1996; Mrsic-Flogel et al., 2007; Scholl et al., 2015), we did not observe any evidence for spatial clustering or microstructure related to eye preference or to CPNs in C57BL/6 mice (**Figure S3**). Both CPNs and non-CPNs showed similar tuning properties for drifting gratings, with only slightly greater orientation selectivity in CPNs (**Figure 1F, Figure S4A, B**). These results suggest that CPNs have somewhat distinct visual response properties from non-CPNs. Although non-CPNs could include interneurons as well as pyramidal neurons with our current approach, we obtained consistent results after correcting the potential influence by the small fraction of interneurons (**Figure S4B**).

CPNs are not organized into columns or spatial clusters in mice (**Figure S3**), but it is still possible that they form functional subnetworks. To test this possibility, we analyzed the signal and noise correlations of CPN and non-CPN activity with unilateral eye stimulation (**Figure 2**) and with drifting grating stimuli (**Figure S4D, E**). Both signal and noise correlations were significantly stronger between CPN pairs than between CPN/non-CPN pairs and non-CPN/non-CPN pairs (**Figure 2B,** CPN/CPN vs. CPN/non-CPN, $P < 0.001$; CPN/CPN vs. non-CPN/non-CPN, $P < 0.001$; **Figure 2E,** CPN/CPN vs. CPN/non-CPN, $P < 0.001$; CPN/CPN vs. non-CPN/non-CPN, $P < 0.001$; n = 62 planes from 7 mice; Friedman test followed by Tukey-Kramer method). These differences also held true when we analyzed neuron pairs of similar soma–soma distance (**Figure 2C** and **F**). Thus, CPNs are likely to form local functional subnetworks that are organized independently of cell body location.

Pairs of V1 neurons showing stronger signal/noise correlation show higher probability of synaptic connections (Cossell et al., 2015; Ko et al., 2011). To directly test whether CPN pairs show higher connection probability, we conducted dual whole-cell patch-clamp recordings from CPNs and/or non-CPNs in slices of the hemisphere contralateral to the CTB injection site at 4–8 days post-injection, specifically targeting the most densely CTB-labeled area in L2/3 (**Figure 3A, B**). We excluded putative interneurons from the analysis of non-CPNs (**see Methods**). Single action potentials in a pyramidal neuron produced EPSCs in a partner neuron in connected pairs (**Figure 3B**). The latency of individual EPSCs was short (mean ± s.d., 1.87 ± 0.49 ms) and the fluctuation of the latency was low (0.2 ± 0.1, coefficient of variation of the latency). No reliable EPSCs with a latency longer than 2.52 ms was observed, indicating that all the recorded EPSCs were monosynaptic currents. The probability of excitatory connections between CPN/CPN pairs (30% of the recorded pairs) was significantly higher than that between CPN/non-CPN pairs (12.2%, $P = 0.046$, Fisher's exact test, **Figure 3C**). The probability of connections between non-CPN/non-CPN pairs (19.1%) also tended to be lower than that of CPN/CPN pairs, although the difference did not reach significance. The connection probability for all recorded pairs (21.1%, 28/133) was in agreement with that for randomly sampled pairs in L2/3 visual cortex (Cossell et al., 2015; Ko et al., 2011). We observed only one reciprocally connected CPN/CPN pair among all the recorded pairs. The overall reciprocal connection probability (0.75%, 1/133) was similar to the expected probability (1.19%, $(29/266)^2$), implying that the establishment of reciprocal connections might be at the chance level regardless of projection targets of neurons in the BZ. The amplitudes of EPSCs recorded from connected CPN/CPN pairs were

comparable to those measured from connected CPN/non-CPN and connected non-CPN/non-CPN pairs ($P = 0.95$, Kruskal–Wallis test, **Figure 3D**). Also, there were no statistical differences in intrinsic membrane properties between CPNs and non-CPNs (**Figure S5)**. Overall, these results demonstrate that L2/3 neurons sharing long-range projection targets form functional subnetworks defined by local connectivity.

Discussion

In the current study, we used CPNs as a model to investigate the functional properties and local circuit organization of long-range projection neurons in the cortex. How CPNs and other projection neurons in the early visual cortex distribute visual feature information in a target-specific manner is an intriguing question. Our data showing stronger signal/noise correlations (**Figure 2**) and local connectivity among CPNs (**Figure 3**) suggest the existence of target-specific local functional subnetworks in L2/3. It has been reported that local subnetworks of neurons sharing similar visual properties emerge through activity-dependent synaptic plasticity (Ishikawa et al., 2014, 2018; Ko et al., 2013). Our data extend these findings by showing that long-range projection specificity is another factor determining local subnetwork organization in L2/3, a notion also supported by a recent study that assessed V1 neurons projecting to different higher visual cortices (Kim et al., 2018). In contrast to the strongly segregated subnetworks found in neurons projecting to different higher-order visual areas within the same hemisphere (Kim et al., 2018), moderately segregated subnetworks between CPNs and non-CPNs reported in the current study may allow for interactions between the subnetworks of CPNs and other neurons in the local network. Overall, this projection target-dependent segregation of local subnetworks may be a general principle for intermingled projection neurons in the mouse cortex. That said, different levels of segregation in distinct projection populations are of note. The extent of segregation would define the selectivity of information to be extracted locally and then transmitted to the projection target.

We found that a larger fraction of CPNs than non-CPNs preferentially responded to ipsilateral eye input. Some of them even showed exclusive ipsilateral eye preference (**Figure 1**). Considering that most of the retino-thalamic afferents cross in the chiasm

(Lund, 1965), and that most of the lateral geniculate neurons show binocular response in rodents (Howarth et al., 2014), this strong ipsilateral selectivity found in CPNs was rather unexpected. This ipsilaterally-biased CPN population may serve to duplicate visual information conveyed by the thalamo-cortical projection, and send a copy of that information to the other hemisphere (Laing et al., 2015). Thus, callosal connections may function as a back-up system for the thalamo-cortical projection (Li et al., 2016). Different from other projection neurons in V1 (Glickfeld et al., 2013), CPNs show similar SPF/TF tuning as non-CPNs (**Figure S5**). This property may also be useful for the putative back-up function. In contrast to our findings, a recent study (Lee et al., 2019) did not find a strongly ipsilaterally biased population (to the hemisphere where CPN somata are located) among callosal inputs to L2/3 V1 neurons (contralateral to the callosal recipient neurons), raising the possibility that the ipsilaterally biased callosal population selectively targets contralateral L5 neurons, which receive the largest fraction of callosal inputs (Petreanu et al., 2007), whereas majority of callosal neurons, which show contralateral eye (to the hemisphere where CPN somata are located) preference, might target contralateral L2/3 neurons.

In the current study, we did not address whether ipsilaterally-tuned CPNs (or more in general, CPNs with similar response properties) selectively tend to show higher connectivity than random CPNs. This is likely the case given the previous findings that similarly tuned neurons tend to be connected in the monocular region of V1 (Cossell et al., 2015; Ko et al., 2011) and that establishment of such fine-scale subnetworks relies on correlated neuronal activity during development (Ishikawa et al., 2014; Ko et al., 2013). It would be an intriguing future study to directly address this point by the post-

hoc slice recording method following *in vivo* imaging (Cossell et al., 2015; Ko et al., 2013; Ko et al., 2011).

Several recent studies have shown that V1 neurons projecting to different higher-order visual cortices (Glickfeld et al., 2013; Matsui and Ohki, 2013) and subcortical areas show distinct response properties (Kim et al., 2015; Lur et al., 2016). However, the extent of overlap through collateral projections (Han et al., 2018) is not known. For instance, CPNs could overlap with other specific projecting populations (Yamashita et al., 2013; Yamashita et al., 2018). Thus, comprehensive characterization of the relationships among projection target, response properties, molecular identity, and local connectivity is required for a better understanding of the circuit logic in the early visual cortex, which functions as a central hub to process visual information.

Funding

This work was supported by grants from CREST-JST (to K.O. and Y.T.), JSPS KAKENHI (Grant number 25221001, 25117004, 19H01006, 19H05642 to K.O., 23500388, 16K06992 to Y.T., 17K14942 to A.W.I), "Neural Diversity and Neocortical Organization" (23123508 and 25123707 to Y.T.) and "Dynamic regulation of brain function by Scrap & Build system" (16H06460 to Y.Y., 17H05745 and 19H04756 to Y. T.), and Brain/MINDS-AMED. K.M.H was supported by Takeda Science Foundation. Y.T. was supported by Astellas Foundation for

Research on metabolic Disorders, the Kodama Memorial Fund for Medical Research, the Novartis Foundation (Japan) for the Promotion of Science and The Uehara Memorial Foundation.

Acknowledgements

We thank D. Hillier (FMI / IOB / HAS), T. Kanamori (University of Basel / UCL-SWC), E.M.M. Meyer (FMI / University of Bristol), and R.K. Morikawa (FMI / IOB) for reading and commenting on earlier versions of the manuscript; T. D. Mrsic-Flogel (University of Basel / UCL-SWC) and P. Znamenskiy (University of Basel / UCL-SWC / Crick) for discussion; all of the members of Ohki laboratory for support and discussion; A. Honda (Ohki lab) for histology; Y. Sono (Ohki lab) for animal care; the Research Support Center, Graduate School of Medical Sciences, Kyushu University for technical support.

Author Contributions

K.M.H. and Y.T. initially conceived the research. K.M.H. designed and performed imaging experiments and analyzed the data. K.O. supervised imaging experiments, data analysis, and interpretation of the data. A.W.I designed and performed slice experiments and analyzed the data. Y.Y. supervised slice experiments, data analysis, and interpretation of the data. K.M.H., Y.T., A.W.I. wrote the manuscript. K.O. and Y.Y commented on the manuscript.

The authors declare no competing interests.

References

Antonini, A., Fagiolini, M., and Stryker, M.P. (1999). Anatomical correlates of functional plasticity in mouse visual cortex. The Journal of neuroscience : the official journal of the Society for Neuroscience *19*, 4388-4406.

Applebury, M.L., Antoch, M.P., Baxter, L.C., Chun, L.L., Falk, J.D., Farhangfar, F., Kage, K., Krzystolik, M.G., Lyass, L.A., and Robbins, J.T. (2000). The murine cone photoreceptor: a single cone type expresses both S and M opsins with retinal spatial patterning. Neuron *27*, 513-

523 523.
524 Berlucchi, G., and Rizzolatti, G. (1968). Binocularly driven neurons in visual cortex of split-
525 chiasm cats. Science *159*, 308-310.
526 Brown, S.P., and Hestrin, S. (2009). Intracortical circuits of pyramidal neurons reflect their
527 long-range axonal targets. Nature *457*, 1133-1136.
528 Cerri, C., Restani, L., and Caleo, M. (2010). Callosal contribution to ocular dominance in rat
529 primary visual cortex. Eur J Neurosci *32*, 1163-1169.
530 Conte, W.L., Kamishina, H., and Reep, R.L. (2009). Multiple neuroanatomical tract-tracing
531 using fluorescent Alexa Fluor conjugates of cholera toxin subunit B in rats. Nat Protoc *4*, 1157-
532 1166.
533 Cossell, L., Iacaruso, M.F., Muir, D.R., Houlton, R., Sader, E.N., Ko, H., Hofer, S.B., and
534 Mrsic-Flogel, T.D. (2015). Functional organization of excitatory synaptic strength in primary
535 visual cortex. Nature *518*, 399-403.
536 Dehmel, S., and Lowel, S. (2014). Cortico-cortical interactions influence binocularity of the
537 primary visual cortex of adult mice. PLoS One *9*, e105745.
538 Drager, U.C. (1974). Autoradiography of tritiated proline and fucose transported
539 transneuronally from the eye to the visual cortex in pigmented and albino mice. Brain Res *82*,
540 284-292.
541 Glickfeld, L.L., Andermann, M.L., Bonin, V., and Reid, R.C. (2013). Cortico-cortical
542 projections in mouse visual cortex are functionally target specific. Nature neuroscience *16*,
543 219-226.
544 Gordon, J.A., and Stryker, M.P. (1996). Experience-dependent plasticity of binocular responses
545 in the primary visual cortex of the mouse. The Journal of neuroscience : the official journal of
546 the Society for Neuroscience *16*, 3274-3286.
547 Govardovskii, V.I., Fyhrquist, N., Reuter, T., Kuzmin, D.G., and Donner, K. (2000). In search
548 of the visual pigment template. Vis Neurosci *17*, 509-528.
549 Hagihara, K.M., Murakami, T., Yoshida, T., Tagawa, Y., and Ohki, K. (2015). Neuronal activity
550 is not required for the initial formation and maturation of visual selectivity. Nature
551 neuroscience *18*, 1780-1788.
552 Han, Y., Kebschull, J.M., Campbell, R.A.A., Cowan, D., Imhof, F., Zador, A.M., and Mrsic-
553 Flogel, T.D. (2018). The logic of single-cell projections from visual cortex. Nature *556*, 51-56.
554 Howarth, M., Walmsley, L., and Brown, T.M. (2014). Binocular integration in the mouse lateral
555 geniculate nuclei. Curr Biol *24*, 1241-1247.
556 Hubel, D.H., and Wiesel, T.N. (1967). Cortical and callosal connections concerned with the
557 vertical meridian of visual fields in the cat. J Neurophysiol *30*, 1561-1573.

Ishikawa, A.W., Komatsu, Y., and Yoshimura, Y. (2014). Experience-dependent emergence of fine-scale networks in visual cortex. The Journal of neuroscience : the official journal of the Society for Neuroscience *34*, 12576-12586.

Ishikawa, A.W., Komatsu, Y., and Yoshimura, Y. (2018). Experience-Dependent Development of Feature-Selective Synchronization in the Primary Visual Cortex. The Journal of neuroscience : the official journal of the Society for Neuroscience *38*, 7852-7869.

Itokazu, T., Hasegawa, M., Kimura, R., Osaki, H., Albrecht, U.R., Sohya, K., Chakrabarti, S., Itoh, H., Ito, T., Sato, T.K.*, et al.* (2018). Streamlined sensory motor communication through cortical reciprocal connectivity in a visually guided eye movement task. Nat Commun *9*, 338.

Kampa, B.M., Letzkus, J.J., and Stuart, G.J. (2006). Cortical feed-forward networks for binding different streams of sensory information. Nature neuroscience *9*, 1472-1473.

Kerlin, A.M., Andermann, M.L., Berezovskii, V.K., and Reid, R.C. (2010). Broadly tuned response properties of diverse inhibitory neuron subtypes in mouse visual cortex. Neuron *67*, 858-871.

Kim, E.J., Juavinett, A.L., Kyubwa, E.M., Jacobs, M.W., and Callaway, E.M. (2015). Three Types of Cortical Layer 5 Neurons That Differ in Brain-wide Connectivity and Function. Neuron *88*, 1253-1267.

Kim, M.H., Znamenskiy, P., Iacaruso, M.F., and Mrsic-Flogel, T.D. (2018). Segregated Subnetworks of Intracortical Projection Neurons in Primary Visual Cortex. Neuron *100*, 1313-1321 e1316.

Ko, H., Cossell, L., Baragli, C., Antolik, J., Clopath, C., Hofer, S.B., and Mrsic-Flogel, T.D. (2013). The emergence of functional microcircuits in visual cortex. Nature *496*, 96-100.

Ko, H., Hofer, S.B., Pichler, B., Buchanan, K.A., Sjostrom, P.J., and Mrsic-Flogel, T.D. (2011). Functional specificity of local synaptic connections in neocortical networks. Nature *473*, 87-91.

Laing, R.J., Turecek, J., Takahata, T., and Olavarria, J.F. (2015). Identification of Eye-Specific Domains and Their Relation to Callosal Connections in Primary Visual Cortex of Long Evans Rats. Cereb Cortex *25*, 3314-3329.

Lee, K.S., Vandemark, K., Mezey, D., Shultz, N., and Fitzpatrick, D. (2019). Functional Synaptic Architecture of Callosal Inputs in Mouse Primary Visual Cortex. Neuron *101*, 421-428 e425.

Li, N., Chen, T.W., Guo, Z.V., Gerfen, C.R., and Svoboda, K. (2015). A motor cortex circuit for motor planning and movement. Nature *519*, 51-56.

Li, N., Daie, K., Svoboda, K., and Druckmann, S. (2016). Robust neuronal dynamics in premotor cortex during motor planning. Nature *532*, 459-464.

593 Lund, R.D. (1965). Uncrossed Visual Pathways of Hooded and Albino Rats. Science *149*,
594 1506-1507.
595 Lur, G., Vinck, M.A., Tang, L., Cardin, J.A., and Higley, M.J. (2016). Projection-Specific
596 Visual Feature Encoding by Layer 5 Cortical Subnetworks. Cell Rep *14*, 2538-2545.
597 Matsui, T., and Ohki, K. (2013). Target dependence of orientation and direction selectivity of
598 corticocortical projection neurons in the mouse V1. Front Neural Circuits *7*, 143.
599 Minciacchi, D., and Antonini, A. (1984). Binocularity in the visual cortex of the adult cat does
600 not depend on the integrity of the corpus callosum. Behav Brain Res *13*, 183-192.
601 Mizuno, H., Hirano, T., and Tagawa, Y. (2007). Evidence for activity-dependent cortical
602 wiring: formation of interhemispheric connections in neonatal mouse visual cortex requires
603 projection neuron activity. The Journal of neuroscience : the official journal of the Society for
604 Neuroscience *27*, 6760-6770.
605 Movshon, J.A., and Newsome, W.T. (1996). Visual response properties of striate cortical
606 neurons projecting to area MT in macaque monkeys. The Journal of neuroscience : the official
607 journal of the Society for Neuroscience *16*, 7733-7741.
608 Mrsic-Flogel, T.D., Hofer, S.B., Ohki, K., Reid, R.C., Bonhoeffer, T., and Hubener, M. (2007).
609 Homeostatic regulation of eye-specific responses in visual cortex during ocular dominance
610 plasticity. Neuron *54*, 961-972.
611 Ohki, K., Chung, S., Ch'ng, Y.H., Kara, P., and Reid, R.C. (2005). Functional imaging with
612 cellular resolution reveals precise micro-architecture in visual cortex. Nature *433*, 597-603.
613 Ohki, K., and Reid, R.C. (2007). Specificity and randomness in the visual cortex. Curr Opin
614 Neurobiol *17*, 401-407.
615 Ohki, K., and Reid, R.C. (2014). In vivo two-photon calcium imaging in the visual system.
616 Cold Spring Harb Protoc *2014*, 402-416.
617 Otsuka, T., and Kawaguchi, Y. (2011). Cell diversity and connection specificity between
618 callosal projection neurons in the frontal cortex. The Journal of neuroscience : the official
619 journal of the Society for Neuroscience *31*, 3862-3870.
620 Payne, B.R., Elberger, A.J., Berman, N., and Murphy, E.H. (1980). Binocularity in the cat
621 visual cortex is reduced by sectioning the corpus callosum. Science *207*, 1097-1099.
622 Peirce, J.W. (2007). PsychoPy--Psychophysics software in Python. J Neurosci Methods *162*,
623 8-13.
624 Petreanu, L., Huber, D., Sobczyk, A., and Svoboda, K. (2007). Channelrhodopsin-2-assisted
625 circuit mapping of long-range callosal projections. Nature neuroscience *10*, 663-668.
626 Ramachandra, V., Pawlak, V., Wallace, D.J., and Kerr, J.N.D. (2020). Impact of visual callosal
627 pathway is dependent upon ipsilateral thalamus. Nat Commun *11*, 1889.

628 Restani, L., Cerri, C., Pietrasanta, M., Gianfranceschi, L., Maffei, L., and Caleo, M. (2009).
629 Functional masking of deprived eye responses by callosal input during ocular dominance
630 plasticity. Neuron *64*, 707-718.
631 Sato, T.K., Hausser, M., and Carandini, M. (2014). Distal connectivity causes summation and
632 division across mouse visual cortex. Nature neuroscience *17*, 30-32.
633 Sato, T.R., Itokazu, T., Osaki, H., Ohtake, M., Yamamoto, T., Sohya, K., Maki, T., and Sato,
634 T.K. (2019). Interhemispherically dynamic representation of an eye movement-related activity
635 in mouse frontal cortex. Elife *8*.
636 Sato, T.R., and Svoboda, K. (2010). The functional properties of barrel cortex neurons
637 projecting to the primary motor cortex. The Journal of neuroscience : the official journal of the
638 Society for Neuroscience *30*, 4256-4260.
639 Schmidt, K.E., Lomber, S.G., and Innocenti, G.M. (2010). Specificity of neuronal responses in
640 primary visual cortex is modulated by interhemispheric corticocortical input. Cereb Cortex *20*,
641 2776-2786.
642 Scholl, B., Pattadkal, J.J., Dilly, G.A., Priebe, N.J., and Zemelman, B.V. (2015). Local
643 Integration Accounts for Weak Selectivity of Mouse Neocortical Parvalbumin Interneurons.
644 Neuron *87*, 424-436.
645 Sterratt, D.C., Lyngholm, D., Willshaw, D.J., and Thompson, I.D. (2013). Standard anatomical
646 and visual space for the mouse retina: computational reconstruction and transformation of
647 flattened retinae with the Retistruct package. PLoS Comput Biol *9*, e1002921.
648 Van Essen, D.C., Anderson, C.H., and Felleman, D.J. (1992). Information processing in the
649 primate visual system: an integrated systems perspective. Science *255*, 419-423.
650 Van Essen, D.C., Newsome, W.T., and Bixby, J.L. (1982). The pattern of interhemispheric
651 connections and its relationship to extrastriate visual areas in the macaque monkey. The Journal
652 of neuroscience : the official journal of the Society for Neuroscience *2*, 265-283.
653 Wang, B.S., Sarnaik, R., and Cang, J. (2010). Critical period plasticity matches binocular
654 orientation preference in the visual cortex. Neuron *65*, 246-256.
655 Wang, Q., and Burkhalter, A. (2007). Area map of mouse visual cortex. J Comp Neurol *502*,
656 339-357.
657 Wiesel, T.N., and Hubel, D.H. (1965). Comparison of the effects of unilateral and bilateral eye
658 closure on cortical unit responses in kittens. J Neurophysiol *28*, 1029-1040.
659 Wunderle, T., Eriksson, D., and Schmidt, K.E. (2013). Multiplicative mechanism of lateral
660 interactions revealed by controlling interhemispheric input. Cereb Cortex *23*, 900-912.
661 Yamashita, T., Pala, A., Pedrido, L., Kremer, Y., Welker, E., and Petersen, C.C. (2013).
662 Membrane potential dynamics of neocortical projection neurons driving target-specific signals.

Neuron *80*, 1477-1490.

Yamashita, T., Vavladeli, A., Pala, A., Galan, K., Crochet, S., Petersen, S.S.A., and Petersen, C.C.H. (2018). Diverse Long-Range Axonal Projections of Excitatory Layer 2/3 Neurons in Mouse Barrel Cortex. Front Neuroanat *12*, 33.

Yoshimura, Y., Dantzker, J.L., and Callaway, E.M. (2005). Excitatory cortical neurons form fine-scale functional networks. Nature *433*, 868-873.

Zhao, X., Liu, M., and Cang, J. (2013). Sublinear binocular integration preserves orientation selectivity in mouse visual cortex. Nat Commun *4*, 2088.

Figures

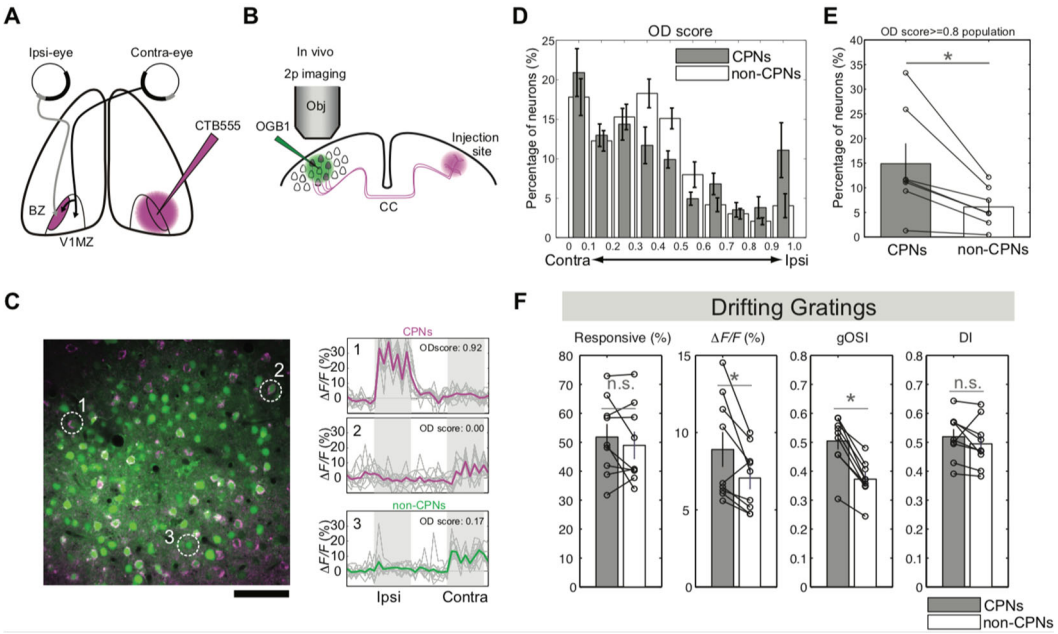

Figure 1. Ocular dominance response properties of CPNs and non-CPNs

A. Schematic drawing of CPNs labeling with retrograde tracer CTB555. BZ: binocular zone; V1MZ: primary visual cortex monocular zone.

B. Schematic drawing of *in vivo* two-photon calcium imaging of CTB555 labeled CPNs and surrounding non-CPNs.

C. (Left) Image of OGB1-labeled (green) and retrogradely CTB555-labeled (magenta) callosal projection neurons (CPNs) and non-CPNs in the binocular zone (BZ). Scale bar: 20 μm. (Right) Representative calcium traces from CPNs (#1 and #2) and a non-CPN (#3) shown in the left panel.

D. Distribution of ocular dominance (OD) scores for CPNs and non-CPNs.

E. Proportion of neurons with an OD score over 0.8. * $P < 0.05$; (n = 7 mice, Wilcoxon signed-rank test)

F. Responsiveness, ΔF/F, gOSI, and direction index (DI) of CPNs and non-CPNs.

*: $P < 0.05$; n.s., non-significant; (Wilcoxon signed-rank test).

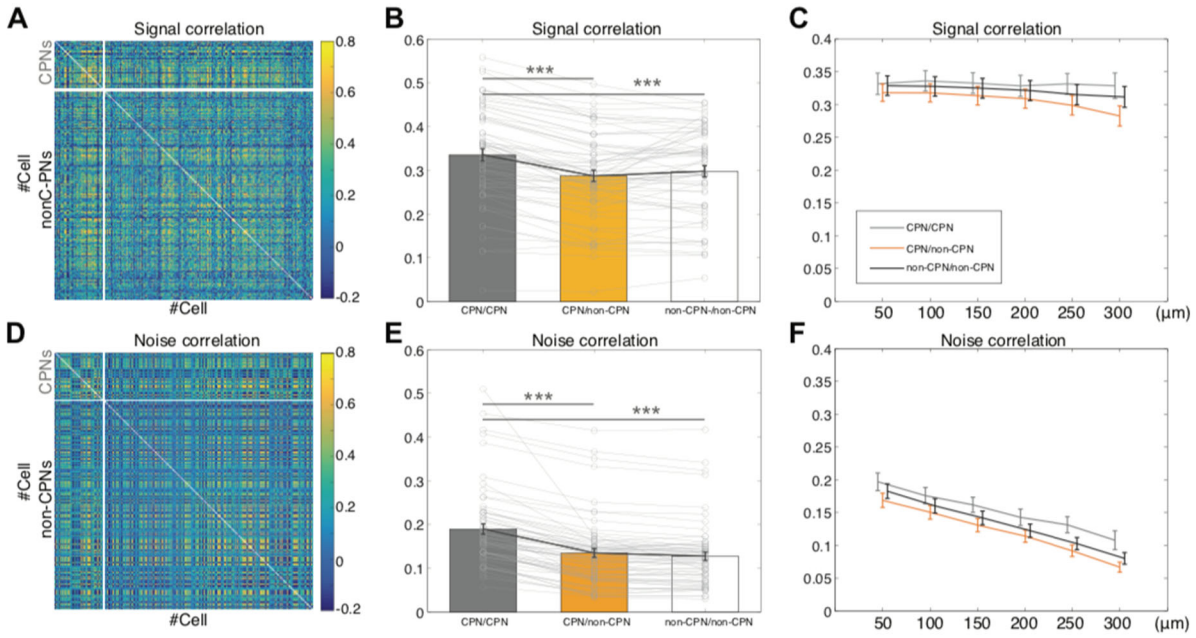

Figure 2. Correlation structure of CPNs and non-CPNs

A, **D**. Representative signal (**A**) and noise (**D**) correlation matrices of neurons from a single imaging plane. The order of neurons is sorted so that CPNs are located at the top and non-CPNs at the bottom.

B, **E**. Means of signal (**B**) and noise (**E**) correlation values from each plane. CPN/CPN pairs show both higher signal and noise correlation coefficient values than CPN/non-CPN and non-CPN/non-CPN pairs.

C, **F**. Signal (**C**) and noise (**F**) correlations of CPN/CPN (gray), CPN/non-CPN (orange), and non-CPN/non-CPN (black) pairs with respect to cortical distance.

***: $P < 1.0 \times 10^{-3}$; (Friedman test followed by Tukey-Kramer).

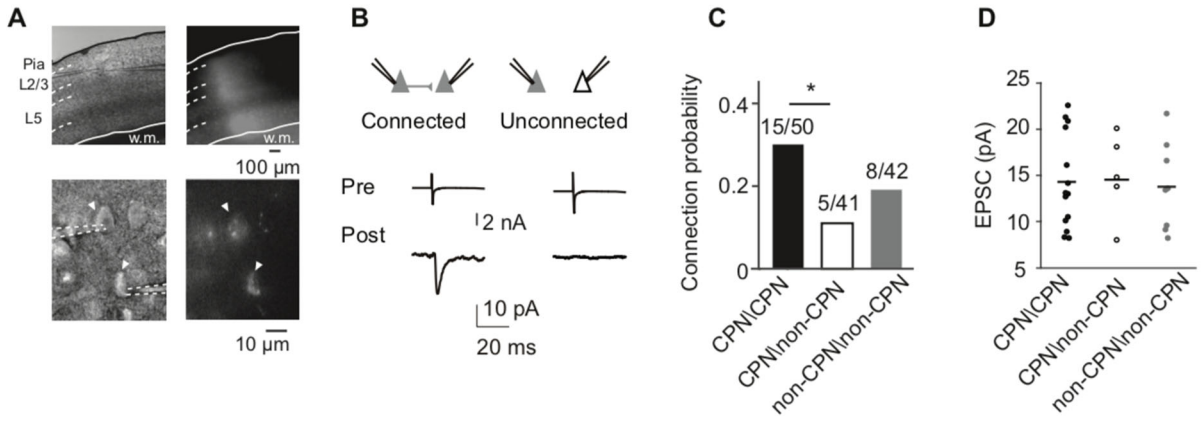

Figure 3. Local synaptic connectivity of CPNs

A. Top-left: Differential interference contrast image showing a recording electrode position in L2/3. Top-right: Corresponding image of CTB fluorescence in a coronal slice of primary visual cortex containing the binocular zone. w.m.: white matter. Bottom-left: Higher magnification of the interference contrast image showing simultaneously recorded neurons (marked with white triangles). Recording pipettes were marked with dotted lines. Bottom-right: Corresponding high-magnification fluorescent image of CTB-labeled CPNs. White triangles mark the same CTB-labeled recorded neurons.

B. Example averaged traces of presynaptic action currents evoked by depolarizing voltage pulses and resultant EPSCs in postsynaptic cells.

C. Connection probabilities of CPN/CPN, CPN/non-CPN and non-CPN/non-CPN pairs. The connection probability of CPN/CPN pairs was significantly higher than that of CPN/non-CPN pairs ($^{*}P < 0.05$ from Fisher's exact test). The numbers of recorded and connected cell pairs are shown above each bar.

D. Amplitudes of evoked EPSCs obtained from connected neuron pairs. Black lines indicate medians.

759

760

761

762

763

764

765